ACS
MATERIALS Au
AN OPEN ACCESS JOURNAL OF THE AMERICAN CHEMICAL SOCIETY

Dynamic Tailoring Porosity and Surface Chemistry of Ultramicroporous Carbon Spheres for Highly Selective Post-combustion CO_2 Capture

Man Liu, Weiwei Shi, Huili Liu, Yanzhen Guo, Baocheng Yang,* and Binbin Chang*

Cite This: *ACS Mater. Au* 2025, 5, 397−408

Read Online

ACCESS | Metrics & More | Article Recommendations | Supporting Information

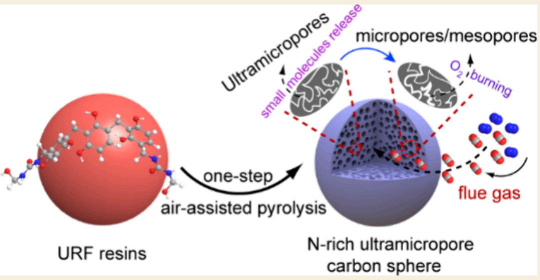

ABSTRACT: Carbon capture has emerged as a pivotal carbon neutrality technology for addressing greenhouse effect challenges. Porous carbons are one of the most promising adsorbents for CO_2 capture and separation from flue gas, yet their traditional synthesis necessitates inert atmospheres to avoid oxidation, which greatly restricts the large-scale production at a low cost and advanced industrial applications. Herein, we propose an innovative pathway for large-scale fabrication of porous carbons via one-step pyrolysis in an air environment. Porosity and surface chemistry can be concurrently tailored by controlling the air-assisted pyrolysis process, and the optimization mechanism is unveiled in detail. The resultant materials feature well-interconnected hierarchical porosity with highly proportioned ultramicroporosity, uniform spherical morphology, and high surface heteroatom doping levels. By leveraging porosity and surface chemistry, the optimal sample exhibits superior CO_2 capture behaviors of satisfactory CO_2 uptake and ultrahigh selectivity. CO_2/N_2 selectivity reaches up to 160 at 0.15 bar and 25 °C, and it still achieves up to 76 at 1.0 bar and 25 °C, ranking it in the top 5% of the reported porous carbons. We explore the correlations between porosity, surface heteroatoms, and CO_2 capture behaviors. Porosity has a decisive function on CO_2 capture capacity and selectivity, especially ultramicroporosity, and surface heteroatoms doping could have a positive promotion in selectivity caused by extra CO_2-philic sites. This work pioneers a feasible approach for large-scale directional design of functional porous carbons through air-assisted pyrolysis under mild conditions.

KEYWORDS: *dynamic tailoring, ultramicroporous, air-assisted pyrolysis, high selectivity, CO_2 capture*

1. INTRODUCTION

Carbon dioxide (CO_2), as the predominant greenhouse gas, arouses global warming and severe environment problems. Currently, for meeting the energy demand of economic development, it is an irresistible difficulty to completely avoid fossil fuel combustion despite the fact that the combustion of fossil fuels results in the continuous rise of atmospheric CO_2 concentration. CO_2 capture, separation, and utilization (CCSU) have been considered a viable technology to mitigate atmospheric CO_2 concentration or reducing CO_2 emission.[1−3] The key to CCSU technology lies in CO_2 capture, which aims at intercepting CO_2 emissions at the point of large-scale industrial generation sources. CO_2 capture by porous solid adsorbents is the most popular approach for CO_2 capture owing to their high adsorption efficiency, simple operation, low energy consumption, and low cost.[4−6]

Among various porous solid adsorbents, porous carbons have been believed to be the highly promising contender by virtue of tailorable porosity, tunable surface environment, simple synthesis, low cost, and easy regeneration.[7−10] In general, materials' textural and chemical properties are interrelated, and thus optimizing the physicochemical properties of porous carbons to leverage their adsorption behaviors remains tremendous challenging. Porosity and surface chemistry play the decisive role in affecting CO_2 capture behaviors of porous carbons.[11−13] Consequently, numerous interests focus on porosity tailoring and surface functionalization to construct porous carbons with high CO_2 uptake and selectivity. As for the pore structure, it has been widely recognized that fine micropores (<1.0 nm) play a crucial role in CO_2 capture capacity especially ultramicropores (<0.7 nm).[14,15] Many efforts have been made to directionally construct porous carbons with a high proportion of narrow micropores via various approaches, such as physical activation, chemical activation, and template methods.[16−18] The engineering of surface functionalization is achieved by heteroatom doping, especially nitrogen doping, which can offer additional CO_2-philic sites to promote CO_2 uptake through acid−based

Received: December 4, 2024
Revised: January 9, 2025
Accepted: January 13, 2025
Published: January 17, 2025

https://doi.org/10.1021/acsmaterialsau.4c00168

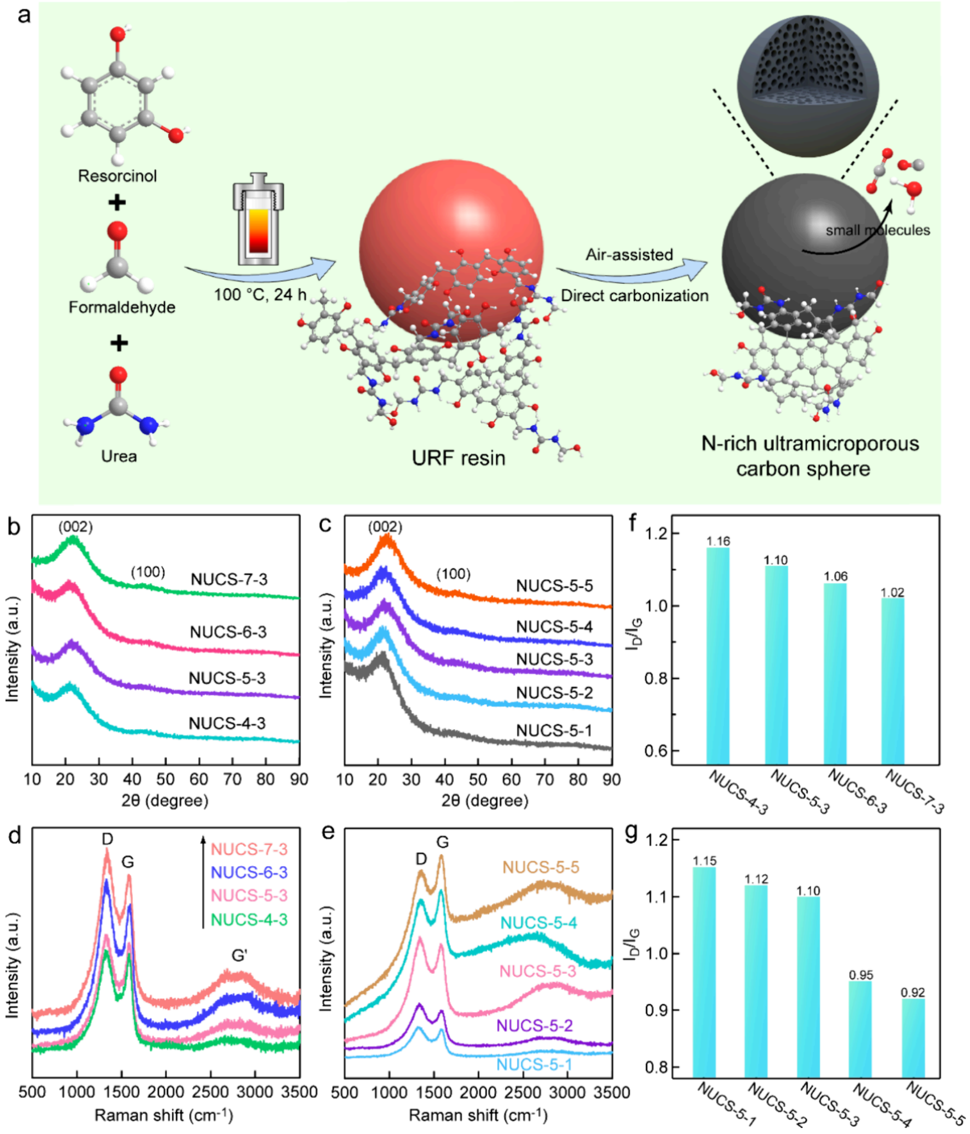

Figure 1. (a) Schematic illustration of the synthesis route and probable formation mechanism of NUCS. Gray ball: C atom; red ball: O atom; blue ball: N atom; white ball: H atom. (b, c) XRD patterns of NUCS-*x*-*y* samples. (d, e) Raman spectra of all NUCS-*x*-*y*. (f, g) The I_D/I_G values of NUCS-*x*-*y* samples.

interactions, hydrogen bonding, and quadrupolar interactions.[19,20] Nitrogen doping is achieved via postmodification involving high-temperature treatment with nitrogen sources and in situ doping of the pyrolysis of nitrogen-containing precursors.[21,22] Unfortunately, these pore controlling strategies above usually necessitate activating agents and templates, which trigger the harsh requirements for equipment, corrosivity, and intricate processes. Moreover, the post-modification of N species often sacrifices porosity caused by pore blocking, and thus developing porosity and surface N doping are mutually competing and incompatible.[23] Particularly noteworthy is the considerable consumption of inert gases in all above synthesis processes,[24] greatly restricting the industrial large-scale production and sustainable application. Therefore, it remains a formidable challenge in the ability to produce porous carbons with high microporosity and an enriched N-doping level on a large scale in an air environment.

For this purpose, we propose a versatile, simple one-step pyrolysis carbonization route in an air atmosphere for the directional design of ultramicroporous carbons on a large scale, which can fine-tune the microporosity and surface chemical environment synchronously. In this route, the cross-linking urea-resorcinol-formaldehyde resins work as carbon precursors owing to rich oxygen-containing and N-containing groups, uniform sphere morphology, and easy large-scale production, and air functions as a coactivator in pyrolysis. Microporosity and surface N species can be leveraged by controlling the pyrolysis process in an air environment. The pore-forming mechanism of the air-assisted pyrolysis method is unveiled in detail. The resultant porous carbons present uniform spherical morphology, well-interconnected and tailorable porosity, high-proportioned ultramicroporosity, and adjustable surface heteroatom doping level. Benefiting from the structural merits, the prepared N-rich ultramicroporous carbon spheres exhibit the outstanding CO_2 capture behaviors of satisfactory CO_2 uptake and high selectivity. Meanwhile, we deeply explore the roles of porosity and surface heteroatoms on CO_2 capture behavior and inform design considerations for improving CO_2 capture capacity and selectivity to effectively capture and separate CO_2 from the simulated flue gas. Our work not only develops a viable pathway for directional synthesis of functional microporous carbons via air-assisted pyrolysis under mild conditions but also provides a possibility for producing porous carbons on an industrial scale.

2. EXPERIMENTAL SECTION

2.1. Chemicals

Resorcinol ($C_6H_6O_2$), urea (CH_4N_2O), formaldehyde (HCHO, 37 wt %), and aqueous ammonia ($NH_3 \cdot H_2O$, 25 wt%) were purchased from Shanghai Aladdin Industrial Corporation. All chemicals are of analytical grade and used without further purification.

2.2. Synthesis of Urea-Resorcinol-Formaldehyde Resins

The resins were synthesized by a Stöber method.[21] Typically, 1.5 mL of aqueous ammonia ($NH_3 \cdot H_2O$, 25 wt%) was added into a mixed solution of 120 mL of absolute ethanol and 300 mL of deionized water. After the mixture was stirred for 30 min at 30 °C, 3 g of resorcinol and 3 g of urea were added into the solution followed by continuous stirring for 30 min. Then, 4.2 g of formaldehyde (HCHO, 37 wt%) was added. After being stirred continuously for 24 h at 30 °C, the mixed solution was placed in a Teflon-sealed autoclave and reacted at 100 °C for 24 h. The products were collected by suction filtration, rinsed with deionized water repeatedly, and oven-dried at 100 °C for more than 10 h to obtain the final resin, which were defined as URF resins.

2.3. Synthesis of N-Rich Ultramicroporous Carbon Spheres

1 g of the dried URF resins was placed in a 25 mL of corundum crucible with a cover and then was pyrolyzed in a muffle furnace at different temperatures (400, 500, 600, and 700 °C) with a heating rate of 5 °C/min. In the pyrolysis process, the cover of the crucible can avoid the products from being polluted or overflowed and at the same time the cover can provide limited air to assist pyrolysis, which can result in a relatively high yield. After the fixed pyrolysis time, the corundum crucible was immediately taken out to cool to room temperature for obtaining the N-rich ultramicroporous carbon spheres. The resultant materials were designated as NUCS-x-y, where $x = 4$, 5, 6, and 7, representing the pyrolysis temperatures of 400, 500, 600, and 700 °C; $y = 1$, 2, 3, 4, and 5, referring to the pyrolysis times of 1, 2, 3, 4, and 5 h.

2.4. Characterizations

X-ray diffraction (XRD) patterns were monitored by a Bruker D8 diffractometer using Cu Kα radiation ($\lambda = 0.15418$ nm) as an X-ray source. Nitrogen adsorption−desorption isotherms were carried out at −196 °C using a Micromeritics ASAP 2020HD88 analyzer. Before adsorption, the samples were outgassed at 200 °C for 10 h. The specific surface area (S_{BET}) was evaluated using the Brunauer−Emmett−Teller (BET) method at the relative pressure of 0.001−0.05, and the pore size distributions were calculated according to the density functional theory (DFT) method. Micropore volumes (V_{micro}) and surface areas (S_{micro}) were analyzed by using the t-plot method. The micropore (<1.0 nm) size distribution and cumulative micropore volume were calculated by fitting the isotherms calculated by DFT to experimental CO_2 adsorption isotherms at 0 °C. The morphology was observed from a scanning electron microscope (SEM, Quanta 250 FEG) and transmission electron microscopy (TEM, FEI Tecnai G2 20). Fourier transform infrared (FTIR) spectra of a sample in a KBr wafer were recorded on a Nicolet Avatar 370 spectrometer. X-ray photoelectron spectra (XPS) were obtained on a VG ESCALAB MK II X-ray photoelectron spectrometer with an exciting source of Mg Kα (1253.6 eV). Raman spectra were recorded on a Raman spectrometer (HORIBA/LabRAM HR Evolution) operating with a 532 nm laser. Dynamic light scattering (DLS) plots were recorded using a Malvern Zetasizer/Nano ZS90.

2.5. Gas Adsorption Measurements

Gas adsorption isotherms of CO_2 and N_2 were measured by using a Micromeritics ASAP 2020HD88 instrument. Highly pure gases CO_2 (99.999%) and N_2 (99.999%) were employed for the measures. The isotherms of CO_2 and N_2 at 0 and 25 °C were conducted in a water bath. Prior to each gas uptake measurement, the samples were degassed at 200 °C for 2 h.

The selectivity for CO_2 from the IAST model was determined from the following equation:

$$S = [p(CO_2)/q(CO_2)]/[p(N_2)/q(N_2)]$$

where S is the selectivity for CO_2, p is the uptake amount of CO_2/N_2, $q(CO_2)$ is 0.15, and $q(N_2)$ is 0.85. The 15/85 CO_2/N_2 ratio used in the calculation represents the typical composition of flue gas.

3. RESULTS AND DISCUSSION

3.1. Physiochemical Property Analysis of Materials

Well-interconnected N-rich ultramicroporous carbon spheres were synthesized via a facile one-step air-assisted pyrolysis strategy, and the synthesis route and probable formation mechanism are illustrated in Figure 1a. First, cross-linked URF resins were obtained through a step-growth hydrothermal polymerization of resorcinol, formaldehyde, and urea, which is a cross-linking mechanism of condensation reaction. A condensation reaction continuously proceeds among the hydroxymethyl groups between the polymerized phenolic resin (RF) and urea-formaldehyde resin (UF) to generate methylene- and methylene ether bridged polymers. Such polymers contain multifunctional branched polymeric monomers, which can copolycondense to grow the spherical URF copolycondensation framework (Figure S1, Supporting Information) under hydrothermal conditions with an increasing cross-linked degree. Noticeably, the polymerization degree greatly depends on the hydrothermal temperature and time, and high temperature and long reaction time bring the discrimination in polymerization degree of URF resins, which results in different sphere diameter sizes. Subsequently, during the carbonization process, the pyrolysis of URF resin spheres can introduce numerous micropores with the release of small molecules and ultramicropores are dominant. As a result, URF resin spheres were converted into carbon spheres with a reduced diameter size due to structural shrinkage. The obtained carbon spheres feature plenty of alicyclic hexatomic spacer-connected benzene rings through the elimination of H_2O molecules, which can also bring the structural shrinkage, and the detailed reaction process and changes in molecular structure are depicted in Figure S2. Moreover, with air assistance, some of the carbons in carbonaceous resin were further burned by the O_2 in air, which produced more pores and even led to an enlarged micropore size. Meanwhile, during the carbon burning process, the generated CO_2/CO gases escaped through the carbon skeleton, which can bring some additional micropores. Consequently, the well-interconnected porosity can be tailored by adjusting the pyrolysis process.

Crystalline structure evolution from URF resins to N-rich ultramicroporous carbon spheres was first characterized by XRD analysis. URF resins show a typical amorphous polymer feature with a wide hump at around 21° (Figure S3). As shown in Figure 1b,c, all NUCS-x-y samples exhibit two weak diffraction peaks at ∼23° and ∼44°, which are assigned to (002) and (100) planes of carbon,[25] respectively. However, the low intensity and wide shape suggest the amorphous carbon framework. The structural defects and graphitization degree of carbon skeleton were further analyzed by Raman spectra (Figure 1d,e). Two narrow peaks at ∼1340 and 1580 cm^{-1} are found in all NUCS-x-y samples, which belong to the D and G bands, respectively. The D band refers to disorder nature of

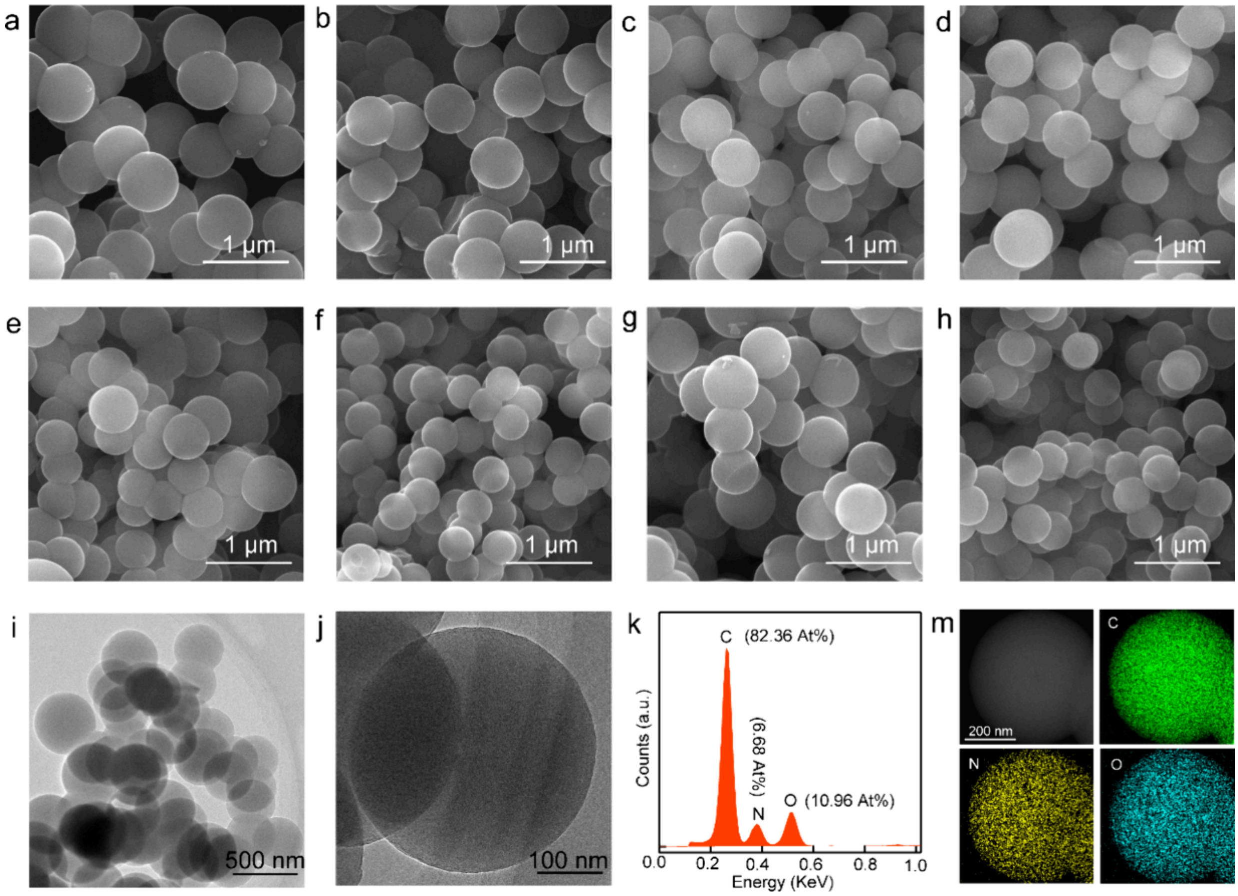

Figure 2. SEM images. (a) NUCS-4−3; (b) NUCS-5−1; (c) NUCS-5−2; (d) NUCS-5−3; (e) NUCS-5−4; (f) NUCS-5−5; (g) NUCS-6−3; (h) NUCS-7−3. TEM images of the representative NUCS-5−3 sample (i and j). EDS analysis (k); C, N, and O elemental mapping images of NUCS-5−3 (m).

carbon, reflecting the structural defects. The G band represents sp^2-bonded graphitic carbon, reflecting the graphitization degree of the carbon skeleton. Generally, the comparative intensity ratio of the D-band and G-band (I_D/I_G) estimates the level of graphitic order in the carbon skeleton. The relatively high I_D/I_G values (Figure 1f,g) indicate the low graphitization degree and poor crystallinity as well as high structural defect degree, which is consistent with the analysis results of XRD. However, it can be clearly found that the graphitization degree of NUCS-*x*-*y* samples enhance with the rise of carbonization temperature and carbonization time, which could be attributed to the sufficient heat energy to progress the graphitic order.[26]

The structural evolution from URF resins to carbon spheres can be revealed by electron microscopy. URF resins present uniform nanospheres with a diameter of ∼800 nm and possess smooth surfaces (Figure S1). After pyrolysis in air, all NUCS-*x*-*y* samples completely retain the spherical morphology, and the surface smoothness also exhibit a negligible change (Figure 2a−h). Noticeably, the sizes of NUCS-*x*-*y* nanospheres are smaller than those of URF resins, and their sizes become smaller with the enhancement of the pyrolysis temperature and time (Figure S4). Such results should be ascribed to the structural shrinkage resulting from the removal of small molecules and the cross-linking rearrangement among polymer chains.[27] As displayed in the SEM image and the DLS (Figure S5), an ∼25% shrinkage in overall particle size is observed in NUCS-4−3, and an around 50% shrinkage is found in NUCS-7−3. The uniform and cross-link spherical aspect with a diameter of ∼500 nm can be further observed in the TEM image of NUCS-5−3 (Figure 2i). Some small white spots can be found in high-magnification TEM images of a single nanosphere (Figure 2j), suggesting the existence of abundant hierarchical micropores. The EDS analysis demonstrates the existence of C, N, and O elements (Figure 2k). Elemental mapping images verify uniform elemental C, N, and O distributions (Figure 2m).

FTIR spectra reveal the compositional evolution from URF resins to NUCS-*x*-*y* samples (Figure S6). For URF resins, relatively abundant surface functional groups can be observed, including −OH groups in adsorbed H_2O molecule (∼3200−3400 cm^{-1}), carbonyl groups (∼1620 cm^{-1}), − CH_2 groups (∼1460 cm^{-1}), C−O−C groups (∼1100−1300 cm^{-1}), and C−N groups (∼1050 cm^{-1}). Obviously, all these groups presented in URF resins almost disappear in all NUCS-*x*-*y* samples, and only two bands at ∼1640 and 1260 cm^{-1} can be found, which are related to C═C and C−C stretching vibration,[28] respectively. Such results demonstrate the partial removal of oxygen-containing and hydrogen-containing groups in the pyrolysis process. The intensity of the C═C and C−C bands gradually enhance with the increase of carbonization temperature and time, suggesting the formation of a better carbon skeleton. The weak −CH_2 stretching vibration peak can be observed in NUCS-4−3, NUCS-5−1, and NUCS-5−2, which indicate that the low temperature and short carbonization time are not sufficient to removal all these groups. Additionally, the weak peak at ∼2200 cm^{-1} in all UNCS-*x*-*y*

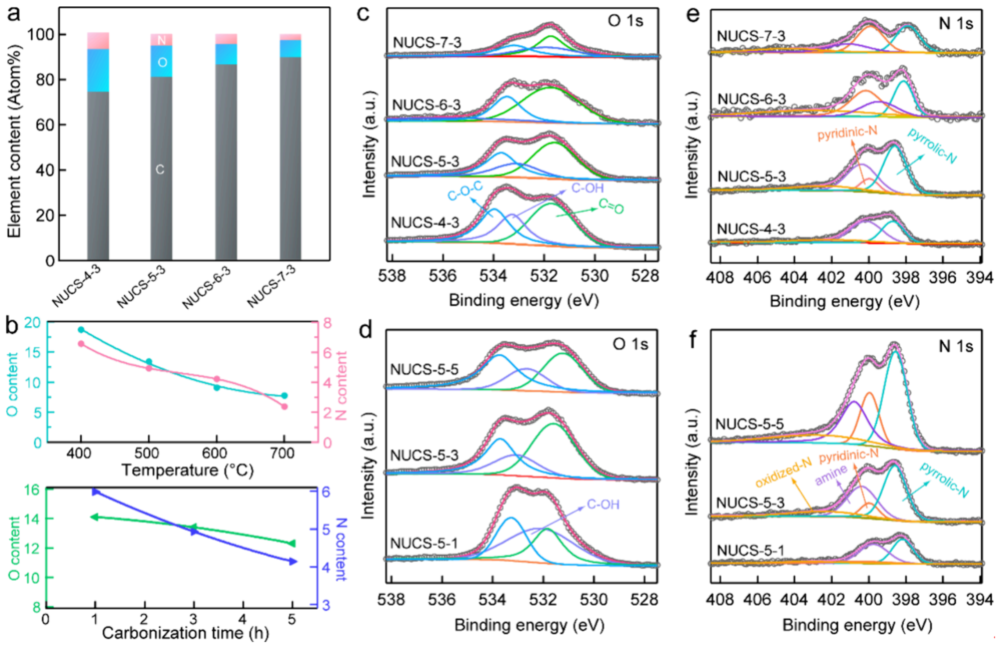

Figure 3. XPS analysis. (a) Elemental contents of C, N, and O in NUCS-*x*-3 samples. (b) The effect of carbonization temperature and time on the O/N contents. (c, d) High-resolution O 1s spectra. (e, f) High-resolution N 1s spectra of NUCS-*x*-*y*.

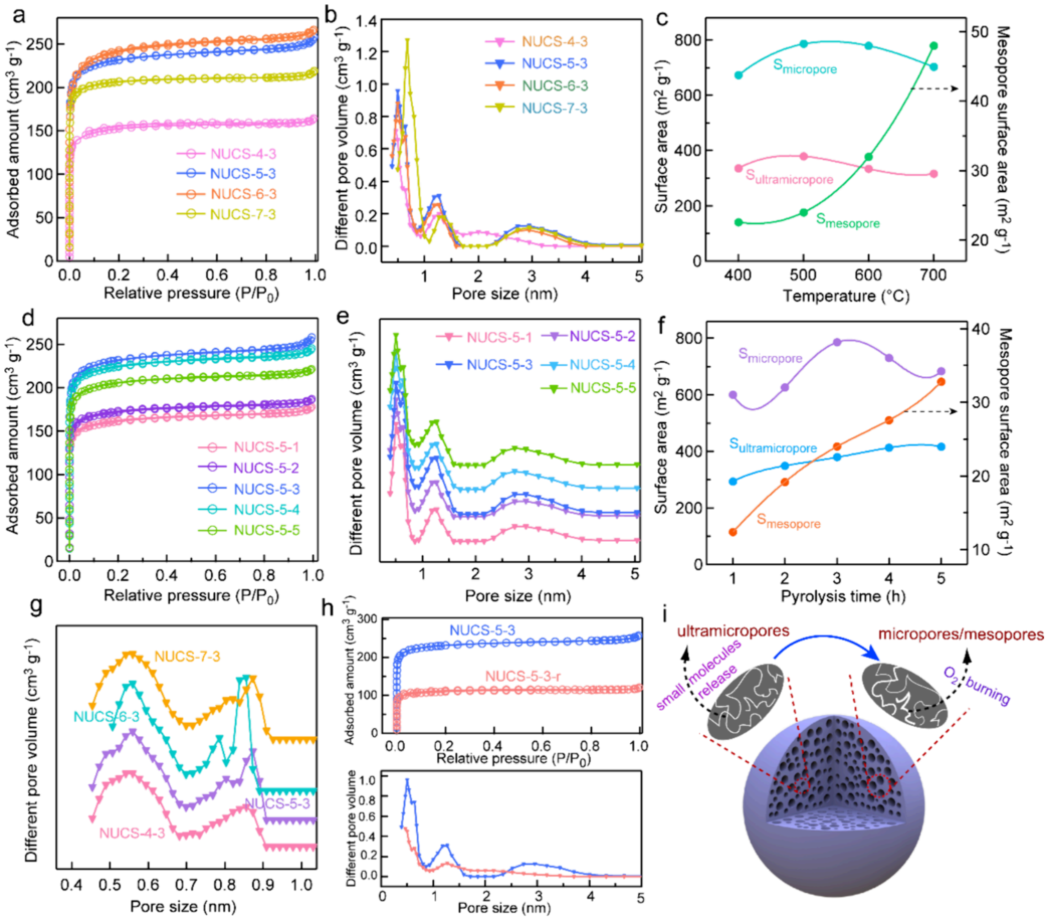

Figure 4. Pore structure analysis. (a) N_2 adsorption−desorption isotherms and (b) pore size distributions of NUCS-*x*-3 samples. (c) The effect of pyrolysis temperature on porosity. (d) N_2 adsorption−desorption isotherms and (e) pore size distributions of NUCS-5-*y* samples. (f) The relationship between activation time and porosity. (g) The micropore (<1.0 nm) size distribution of NUCS-*x*-3 measured by CO_2 adsorption at 0 °C. (h) Comparison of pore structure of materials carbonized in N_2. (i) The air-assisted activation mechanism analysis.

Table 1. Pore Textural Parameters of All the As-Obtained Samples

sample	S_{BET}[a] ($m^2\ g^{-1}$)	S_{micro}[b] ($m^2\ g^{-1}$)	S_{ultra}[c] ($m^2\ g^{-1}$)	V_{total}[d] ($cm^3\ g^{-1}$)	V_{micro}[e] ($cm^3\ g^{-1}$)	V_{ultra}[f] ($cm^3\ g^{-1}$)	yield (wt%)
NUCS-4−3	695.1	672.5	335.7	0.31	0.27	0.10	48
NUCS-6−3	811.3	790.1	333.9	0.35	0.32	0.11	25
NUCS-7−3	750.3	736.9	315.7	0.32	0.30	0.09	19
NUCS-5−1	612.8	600.4	293.9	0.26	0.24	0.09	61
NUCS-5−2	645.3	626.1	349.1	0.28	0.25	0.10	49
NUCS-5−3	809.6	785.6	379.2	0.35	0.32	0.11	36
NUCS-5−4	758.5	740.9	412.8	0.33	0.30	0.12	28
NUCS-5−5	716.2	683.4	416.7	0.30	0.14	0.12	24

[a]BET surface area. [b]Micropore surface area calculated using the *V*−*t* plot method. [c]Ultramicropore surface area calculated using the DFT method to experimental CO_2 adsorption at 0 °C. [d]The total pore volume calculated by single point adsorption at $P/P_o = 0.9945$. [e]The micropore volume calculated using the *V*−*t* plot method. [f]Ultramicropore volume calculated using DFT method to experimental CO_2 adsorption at 0 °C.

samples could be ascribed to the presence of C≡N bonds.[29] The transformation of the surface chemistry surroundings was further confirmed by XPS characterization. The survey spectra further confirm the main elemental composition of C, N, and O in NUCS-*x*-*y* (Figure S7), and the elemental contents of C, N, O are summarized in Figure 3a and Figure S8. As shown in Figure 3b, the N and O elemental contents gradually decrease with the increasing pyrolysis temperature and time, further testifying to the thermal removal of partial hydroxyl and carbonyl groups in pyrolysis, which are consistent with the results of FTIR analysis. Furthermore, it can be found that pyrolysis temperature has a greater influence on the decrease of N and O contents than pyrolysis time. The high-resolution O 1s spectra further analyze the bonding information on surface oxygen species. Three main peaks can be detected at approximately 531.6, 533.3, and 533.8 eV (Figure 3c,d), which are assigned to the C═O, C−OH, and C−O−C groups, respectively. Quantitatively, the proportion of the C−OH group in all NUCS-*x*-*y* samples decreases with the rise of temperature and the increase of pyrolysis time, further demonstrating the elimination of surface hydroxyl groups in pyrolysis. Overall, C═O groups have a higher proportion than those of other oxygen species in all NUCS-*x*-*y* samples except NUCS-5−1. Generally, the main nitrogen species doped in the carbon framework are pyridinic-N (C═N−C), pyrrolic N (C−NH−C), graphitic N (CN), amine (−NH_2), and oxidized N (N−O),[30] and the schematic diagram is depicted in Figure S9. The high-resolution N 1s spectra reveal the presence of four different nitrogen species located at 398.6, 400.2, 401.2, and 402.6 eV (Figure 3e,f), corresponding to pyrrolic-N, pyridinic-N, and amine and oxidized N, respectively. Apparently, the proportions of pyrrolic N and amine are dominant in NUCS-4−3 and NUCS-5-*y* samples. However, the proportions of pyrrolic-N and pyridinic-N are dominant in NUCS-6−3 and NUCS-7−3 samples, which could be ascribed to the elimination of partial amine in high pyrolysis temperature.[31] Such results are consistent with the reaction process (Figure S2).

The evolution of the porous texture of NUCS-*x*-*y* samples was evaluated by N_2 sorption technology. Figure 4a presents the N_2 adsorption−desorption isotherms of NUCS-*x*-3 samples with different pyrolysis temperature. All NUCS-*x*-3 samples exhibit a type I isotherm, indicating a microporous structure, and these micropores should be mainly from the elimination of surface oxygen-containing and hydrogen-containing groups or the pyrolysis of small molecules. Furthermore, it can be clearly found that the N_2 adsorbed amount presents a stepwise increase at the high pressure region of close 1.0, manifesting the existence of mesopores,[32] which could be caused by the coalescence of some micropores under high heat energy or air-assisted activation. The high N_2 adsorbed amount at a low relative pressure of less than 0.01 means a large micropore surface area, and the higher N_2 adsorbed amount with the rise of pyrolysis temperature suggests the larger micropore surface area (Table 1). Additionally, there is an adsorption knee in all isotherms, and the balance adsorption inflection points gradually prolongs to the high pressure region with the increasing pyrolysis temperature, which suggest the enlargement of some micropores.[33] Pore size distribution can further reveal the evolution of the pore structure. As depicted in Figure 4b, the micropores of NUCS-4−3 mainly center at 0.47 nm, a small amount of micropores locate at 1.18−1.27 nm, and a small amount of mesopores are in 2.01 nm. In addition, it can be observed that micropores of 0.64 nm begin to produce in NUCS-4−3. NUCS-5−3 and NUCS-6−3 are still microporous, and their micropores mainly center at 0.50 nm, and the 0.64 and 1.18−1.27 nm of micropores obviously increase. As the pyrolysis temperature rises to 700 °C, most of the micropores enlarge to 0.68 nm, and 1.18−1.27 nm of micropores is enlarged to 1.27−1.46 nm. Meanwhile, the mesopores widen to approximately 3.0 nm. Such results should be ascribed to further pyrolysis and activation under high heat energy. Figure 4c summarizes the influence of the pyrolysis temperature on porosity. With the increase of pyrolysis temperature, S_{micro} and S_{ultra} gradually increase and then slowly decrease, but S_{meso} continuously increases. High temperature can bring enough heat energy to favor the deep pyrolysis and activation reactions, which results in the enhancement of S_{micro} and S_{ultra}. Some micropores continuously enlarge and even coalesce to form mesopores under higher heat energy, and thus lead to the slow decrease of S_{micro} and S_{ultra} as well as the continuous increase of S_{meso}. Such results confirms the vital role of pyrolysis temperature on the tailoring of porosity.

Activation time is another critical parameter for tailoring the porosity. Similar to the NUCS-*x*-3 samples, all NUCS-5-*y* also show a type I isotherm of microporous structure (Figure 4d). As displayed in the pore size distribution (Figure 4e), a hierarchical pore size can be found in all NUCS-5-*y* samples with dominant ultramicropores centered at 0.50−0.64 nm, supermicropores at 1.18−1.27 nm, and also mesopores at 2.17−4.0 nm. Figure 4f depicts the relationship between the porosity and pyrolysis time. Apparently, S_{micro} gradually increases with an increase of pyrolysis time from 1 to 3 h and then decreases as the pyrolysis time increased from 3 to 5 h. S_{ultra} shows a continuous increase with a slow rate after 3 h.

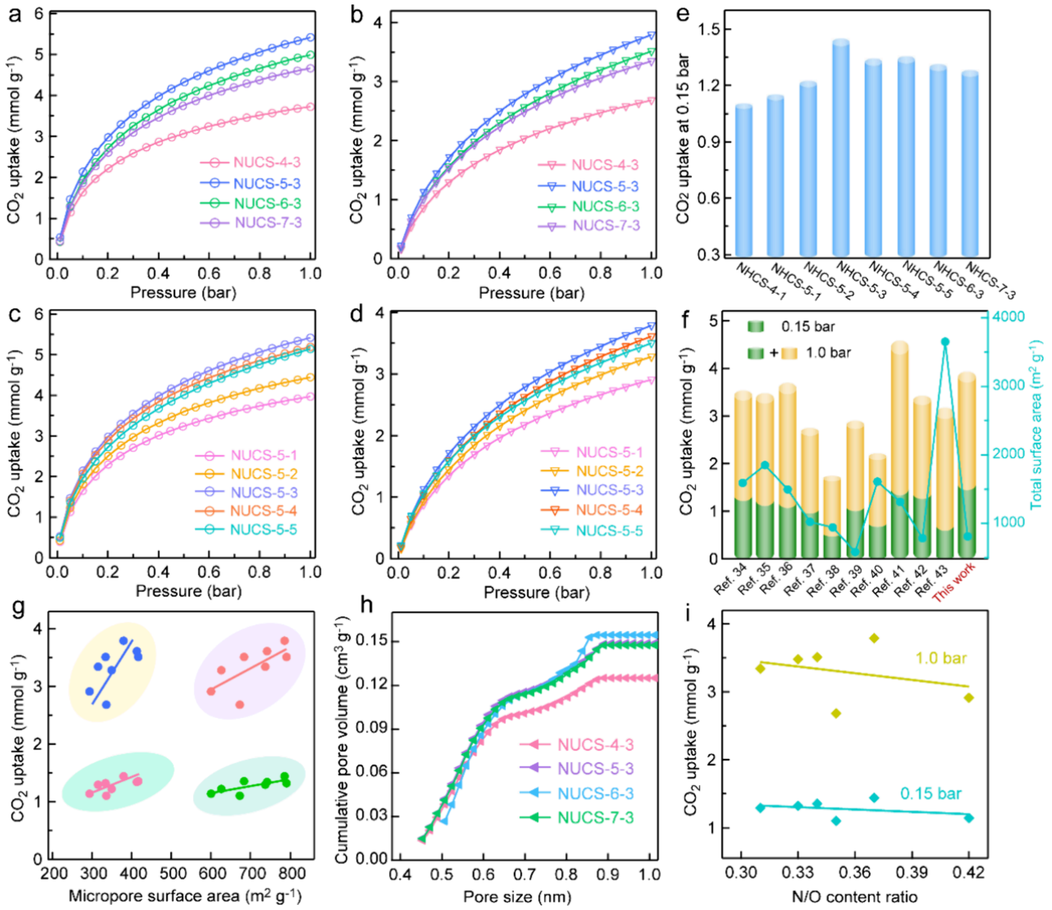

Figure 5. CO_2 capture performance. CO_2 adsorption isotherms over NUCS-*x*-3 at 0 °C (a) and 25 °C (b). CO_2 adsorption isotherms over NUCS-3-*y* at 0 °C (c) and 25 °C (d). (e) CO_2 uptake at 0.15 bar and 25 °C. (f) The comparison of CO_2 uptakes over different porous carbon adsorbents at 25 °C. (g) Relationship between CO_2 uptake at 25 °C and surface area. Pink dot: CO_2 uptakes are at 0.15 bar and S_{ultra}. Green dot: CO_2 uptakes at 0.15 bar and S_{micro}. Blue dot: CO_2 uptakes at 1.0 bar and S_{ultra}. Orange dot: CO_2 uptakes at 1.0 bar and S_{micro}. (h) The cumulative micropore of <1.0 nm volume. (i) The correlation between N/O content ratio and CO_2 uptakes at 25 °C.

In contrast, S_{meso} presents a sharp enhancement with an increasing pyrolysis time. The inadequacy of heat energy at 500 °C cannot favor the complete pyrolysis reaction, and thus ultramicropores are continuously generated with prolonging activation time. However, some produced micropores can be enlarged to form mesopores under air assistance, and thus S_{micro} begins to decrease as pyrolysis time increases to 3 h. The detailed pore structure properties of all of the resultant NUCS-*x*-*y* materials are summarized in Table 1. Based on these pore structural parameters, it can be concluded that porosity can be effectively tailored by tuning the pyrolysis temperature and time under the air-assisted activation.

To further explore the porosity, micropores less than 1.0 nm were analyzed using CO_2 adsorption at 0 °C with the density functional theory (DFT) method, which provides more information about the accessible micropores, especially ultramicropores. Different from the micropore size distribution measured by N_2 adsorption, a multiscale micropore size distribution can be obtained in all NUCS-*x*-*y* by CO_2 adsorption (Figure 4g and Figure S10). These fine micropores contain 0.45−0.70 nm ultramicropores and 0.75−0.90 nm supermicropores, in which ultramicropores are dominant. With the rise of pyrolysis temperature and time, some ultramicropores (<0.7 nm) are enlarged to form supermicropores (0.7−2.0 nm),[32] bringing the enhancement of supermicropores proportion.

To ascertain the pore generation mechanism in air-assisted pyrolysis, we compare the porous structure of NUCS samples pyrolyzed in a N_2 atmosphere (NUCS-*x*-*y*-r). In the absence of air, the NUCS-5−3-r sample exhibits a typical micropore structure with a lower surface area of 424.2 $m^2\ g^{-1}$ (Figure 4h). By comparing the pore size distribution, NUCS-5−3-r has dominant micropores smaller than 0.5 nm without any mesopores, which is much poorer than the multiscale pore size distribution observed in NUCS-5−3. Prolonging the pyrolysis time from 3 to 5 h in N_2 results in only a slight increase in total surface area, with no changes observed in pore size distribution except for an increased proportion (Figure S11a,b). Similarly, when the pyrolysis temperature is elevated to 700 °C in N_2, the total surface area also exhibits a slight increase, and only micropores of approximately 0.75 nm are present in NUCS-7−3-r (Figure S11c,d). Based on the above analysis results, we propose a plausible air-assisted pyrolysis mechanism (Figure 4i), where (i) the pyrolysis of initial resins generates numerous ultramicropores due to small molecules release; (ii) under the assistance of an air atmosphere, some ultramicropores further develop into micropores; and (iii) even some micropores continuously enlarge into mesopores by the further burning of the partial carbon skeleton with O_2 in air.

3.2. CO_2 Capture Property

In view of the well-interconnected porosity with a large proportion of ultramicropores and rich surface functional groups, the resultant NUCS-*x*-*y* materials are believed to be a promising adsorbent for CO_2 capture. Isothermal CO_2 capture investigations of NUCS-*x*-*y* were carried out at two temperatures of 0 and 25 °C with a pressure up to 1 bar. As depicted in Figure 5a−d, the CO_2 capture capacity of all NUCS-*x*-*y* samples continuously increase up to 1 bar pressure at two test temperatures, which indicates that the saturation adsorption point has not been reached, meaning the superior CO_2 uptake at higher pressure. However, it is obvious that the gradients of CO_2 adsorption isotherms of all materials are more pronounced at lower pressures, while the increase trend in CO_2 uptakes decelerates with further increase of pressure. Furthermore, the CO_2 uptakes of all samples show a decrease with the rise of adsorption temperature, which confirms that the CO_2 adsorption is an exothermic physical adsorption process. The CO_2 uptakes at different pressures and temperatures are summarized in Table 2. NUCS-4−3 presents the CO_2 uptakes of 3.72 mmol g^{-1} at 0 °C and 2.68 mmol g^{-1} at 25 °C under 1 bar. With increasing pyrolysis temperature, NUCS-5−3 exhibits superior CO_2 uptakes of 5.42 and 3.79 mmol g^{-1} at 0 and 25 °C under 1 bar, respectively, which should be ascribed to its improved porosity. However, the further increase in the pyrolysis temperature brings a continuous decrease in CO_2 uptakes (Table 2), which could be related to the change in porosity. After comparison, though NUCS-6−3 has a total surface area similar to that of NUCS-5−3, it has a lower ultramicropore surface area (Table 1), which results in a decline in CO_2 uptake. Such results demonstrate the decisive role of ultramicropores in CO_2 capture. Furthermore, a similar tendency can be found between the pyrolysis time and CO_2 uptakes (Figure 5c,d). NUCS-5−4 and NUCS-5−5 have a higher ultramicropore surface area, but they exhibit a lower CO_2 uptake than NUCS-5−3, which could be attributed to their lower total surface area or surface N functional groups contents.

Table 2. CO_2 Uptakes of NUCS-*x*-*y* at Different Temperatures and Pressures

	CO_2 uptake (mmol g^{-1})			
sample	0.15 bar, 0 °C	1.0 bar, 0 °C	0.15 bar, 25 °C	1.0 bar, 25 °C
NUCS-4−3	1.96	3.72	1.10	2.68
NUCS-5−1	2.01	3.97	1.14	2.91
NUCS-5−2	2.19	4.44	1.22	3.28
NUCS-5−3	2.62	5.42	1.44	3.79
NUCS-5−4	2.52	5.18	1.34	3.61
NUCS-5−5	2.38	5.14	1.35	3.51
NUCS-6−3	2.37	4.99	1.32	3.51
NUCS-7−3	2.27	4.66	1.29	3.34

The practical pressure of CO_2 in postcombustion flue gases is about 0.15 bar, and thus the CO_2 capture capacity of adsorbents at 0.15 bar is a vital parameter to estimate its practical application potential. As shown in Figure 5e, NUCS-5−3 shows the largest CO_2 uptake of 1.44 mmol g^{-1} at 0.15 bar and 25 °C, which could be related to its high microporosity, especially high ultramicroporosity. NUCS-5−4 and NUCS-5−5 display a slight decline in CO_2 uptake at 0.15 bar, which could result from their poor surface functional groups. According to the above analysis, it can be concluded that the outstanding CO_2 capture property should be determined by the synergistic effect of ultramicroporosity, microporosity, surface functional groups, and pore size distribution. Such CO_2 capture capacity is comparable and even better than those of most porous carbon-based adsorbents (Figure 5f).[34−43]

To better understand the effect of porosity and surface functional groups on the CO_2 capture capacity, we further analyze the relationship between porosity and CO_2 uptake in detail. The weak positive correlations between CO_2 uptakes and total surface area and total pore volume can be found (Figure S12), which suggest that superior porosity has a promotion on the CO_2 capture property, especially CO_2 uptakes at 0.15 bar. According to the kinetic adsorption mechanism, narrow micropores of less than 1.0 nm play a crucial role for CO_2 capture.[44,45] As a result, we further analyze the correlation of CO_2 uptakes and micropores surface area in different pore size ranges (Figure 5g). Obviously, the ultramicropore surface area and CO_2 uptakes at 0.15 bar show a better correlation, and such results confirm that the favorable pore sizes for CO_2 adsorption centered at ultramicropores of less than 0.7 nm. The cumulative ultramicropore volume further demonstrates the decisive role of ultramicropores on the CO_2 capture property (Figure 5h and Figure S13), and a higher ultramicropore volume usually favors a better CO_2 capture capacity.

Surface chemistry also has a significant effect on the adsorption of CO_2 ions, especially surface heteroatoms. Nitrogen heteroatoms are a typical alkaline CO_2-philic site, which can bring more extra adsorption sites for capturing CO_2 by acid−base interaction. However, a poor correlation is obtained between the total N content and the CO_2 uptakes at different adsorption conditions (Figure S14a,b). Oxygen heteroatoms are another effective site for improving CO_2 capture through hydrogen bonding or polarization.[46,47] Similarly, there is no specific correlation between the total O content and CO_2 uptakes (Figure S14c,d). Furthermore, we further evaluate the relationship between the total heteroatom content and CO_2 uptakes (Figure 5i). Although there is also no apparent correlation between the total heteroatoms amount and CO_2 uptakes, the correlation between heteroatom content and CO_2 uptakes at 0.15 bar is improved, which indicates that heteroatoms could provide some contributions for selective trapping of CO_2 molecules. Such results could be attributed to the variation of porosity caused by the change of surface heteroatoms amount. Meanwhile, surface heteroatoms indeed play a positive role in CO_2 adsorption, especially when the porosity of adsorbents is similar.

Apart from the superior CO_2 uptake, the high selectivity is also vital for adsorbents to meet practical applications in capturing CO_2 from the postcombustion flue gas. In general, the flue gases contain a large number of N_2. Therefore, the superior selectivity of CO_2 capture over N_2 is essential for adsorbents in flue gas adsorption and separation. To test the selectivity of NUCS-*x*-*y* materials, the N_2 and CO_2 adsorption isotherms were measured at 0 and 25 °C. As depicted in Figure 6a and Figure S15, an extremely low N_2 uptake was obtained in all NUCS-*x*-*y* samples, which is much lower than that of CO_2 uptake in the same adsorption condition. Such results indicate the weak interaction of N_2 molecules with the surface of NUCS-*x*-*y*, which favors the highly selective adsorption of CO_2 from the flue gas. Based on the CO_2 and N_2 adsorption

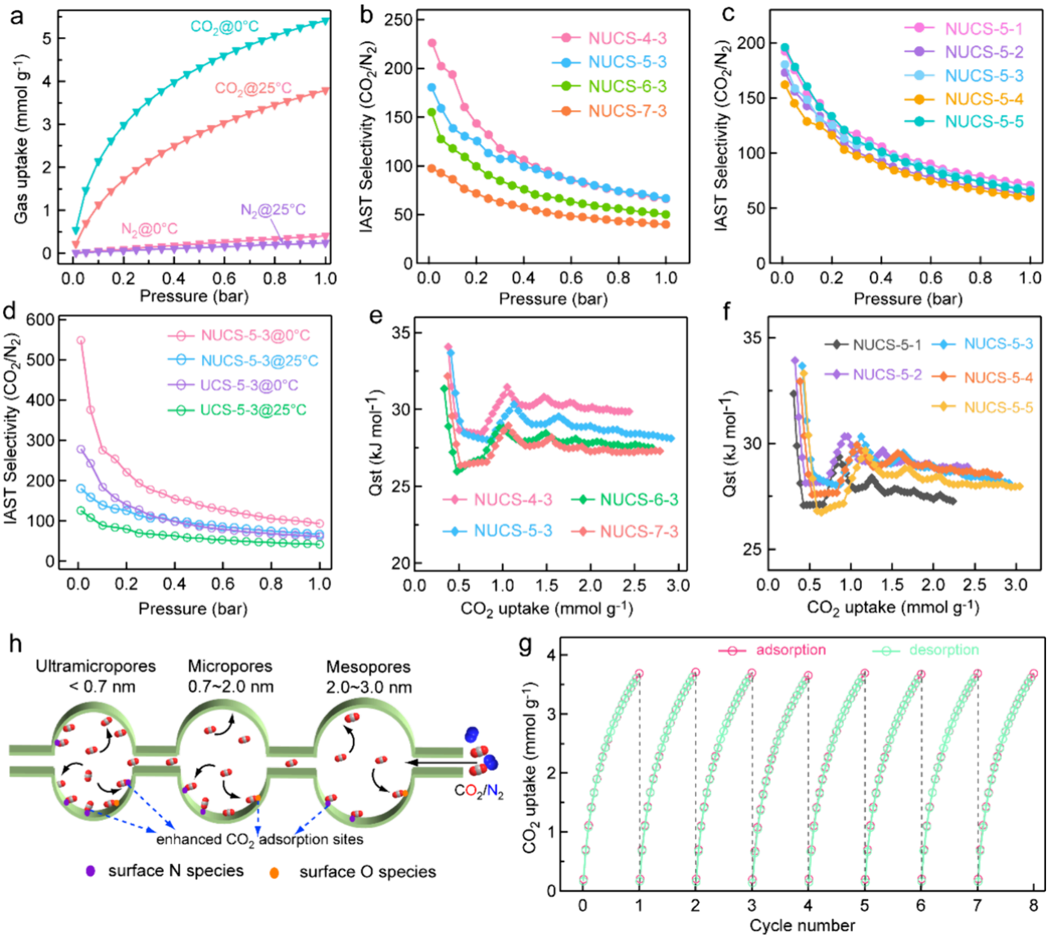

Figure 6. (a) CO_2 and N_2 adsorption isotherms of NUCS-5−3 at various temperatures. (b, c) IAST CO_2/N_2 selectivity of NUCS-*x*-*y* samples at 25 °C. (d) The comparisons of selectivity of NUCS-5−3 with UCS-5−3 at different temperatures. (e, f) Isosteric heat of the CO_2 adsorption of NUCS-*x*-*y*. (g) The recyclability of the NUCS-5−3 sample tested at 25 °C. (h) Schematic diagram of the CO_2 capture mechanism of NUCS-*x*-*y* materials.

isotherms, the CO_2/N_2 selectivity of NUCS-*x*-*y* is calculated using the ideal adsorbed solution theory (IAST). IAST is a well-established model for evaluating the selectivity of nanoporous materials in binary and multicomponent gas mixtures.[48] A 15/85 (v/v) CO_2/N_2 ratio is used for calculating IAST CO_2/N_2 selectivity, which simulates the practical composition of the postcombustion flue gas. The calculated IAST CO_2/N_2 selectivities of NUCS-*x*-*y* are displayed in Figure 6b,c and Figure S16. Evidently, the IAST selectivity shows a sharp decrease in the low-pressure region and then almost achieves a plateau at the high-pressure region, which could be ascribed to the competitive adsorption of CO_2 and N_2 at different adsorption sites. NUCS-4−3 exhibits an ultrahigh CO_2/N_2 selectivity of 160 at 0.15 bar and 25 °C, and a satisfactory selectivity of 76 is still reached at 1.0 bar and 25 °C. Though its porosity is not best, NUCS-4−3 has the best CO_2/N_2 selectivity. Such results could be related to its high surface heteroatom content, which could bring an improvement in selectivity by increasing chemical interactions with CO_2, especially in low pressure region. Noticeably, NUCS-5−3 shows a comparable and even higher selectivity in the high pressure region, which should be ascribed to its superior porosity. It can be concluded that porosity and surface chemistry have a synergistic effect on selectivity. Such a conclusion can be further confirmed by comparing the selectivity of ultramicroporous carbon spheres without surface N species (Figure 6d). However, the effect of surface heteroatoms (N and O species) on selectivity is limited, and porosity could play a better improvement, which can be verified by samples with similar surface N contents but poor porosity. Benefited from the suitable surface N species and prominent porosity, the resultant NUCS-*x*-*y* materials exhibit ultrahigh CO_2/N_2 selectivity, which are much higher than those of other porous carbon-based adsorbents (Figure S17). Such results demonstrate that NUCS-*x*-*y* materials are promising adsorbents for gas adsorption and separation from the practical flue gas.

The incorporation of N and O species can change the surface chemistry environment of carbon adsorbents, which affects the interaction between carbon surface and gas molecules via a complex mechanism, resulting in a non-ignorable influence on CO_2 capture. To reveal the interaction strength of CO_2 molecules and the carbon surface and obtain a better understanding of the CO_2 capture process, the isosteric heat of adsorption (Q_{st}) was calculated from the isotherms at 0 and 25 °C by the Clausius−Clapeyron equation.[49] As illustrated in Figure 6e,f, all Q_{st} values of NUCS-*x*-*y* show a fluctuation with the increasing CO_2 surface coverage and finally achieve a plateau at a high CO_2 surface coverage, which suggests the heterogeneity of the CO_2 capture process. At low CO_2 loading, all Q_{st} ions display a sharp drop, which should be due to the continuous occupancy of the optimal adsorption sites originating from the surface N species and ultramicropores. The initial Q_{st} values of NUCS-*x*-*y* at the low CO_2 coverage are in the range of 31−34 kJ mol^{-1}, which confirms the physical adsorption process. Though NUCS-4−3 has poor porosity, it presents a higher Q_{st} value, which could benefit from its largest surface heteroatom content. Moreover, the Q_{st} values decline with the reduction of surface N species (Figure 6e), which should be ascribed to the strong dipole−quadrupole interactions with CO_2, bringing about the enhancement of Q_{st}. Such results further demonstrate that surface doping heteroatoms have an important effect on CO_2 capture as efficient heterogeneous adsorption sites, which is consistent with the selectivity. Additionally, porosity has a great influence on Q_{st} values at high CO_2 coverage (Figure 6f), especially ultramicroporosity, manifesting a greater contribution of narrow micropores in capturing CO_2. Although a high Q_{st} is essential for CO_2 capture, the extremely high Q_{st} impedes the regeneration of adsorbents, which could greatly limit large-scale industrial application. As a result, a moderate Q_{st} value of the adsorbent is more expected for CO_2 capture and separation in practical applications. As depicted in Figure 6g, almost unchanged CO_2 uptakes are obtained even after eight successive CO_2 adsorption−desorption cycles at 25 °C, demonstrating the excellent regeneration and stability of NUCS-5−3. Considering the superior CO_2 capture behavior, including satisfactory CO_2 uptake, high selectivity, moderate Q_{st}, and good regeneration, the as-obtained NUCS-*x*-*y* materials are believed to be promising adsorbents for effective CO_2 capture and separation.

According to the above analysis of the CO_2 capture behavior, we propose a reasonable adsorption mechanism in NUCS-*x*-*y*, as illustrated in Figure 6h. The Langmuir model aligns well with experimental data of the CO_2 adsorption isotherm (Figure S18), which suggests that the pore-filling of CO_2 molecules in NUCS-*x*-*y* is a monolayer adsorption process. NUCS-*x*-*y* materials have a well-interconnected hierarchical pore structure with highly proportioned micropores. Ultramicropores offer decisive contributions, which are more attractive to capture CO_2 molecules. Micropores of 0.7−2.0 nm act as the secondary adsorption sites for trapping CO_2. Small amounts of mesopores can provide limited adsorption sites, but these interconnected mesopores can facilitate CO_2 molecule transport and diffusion, promoting the CO_2 adsorption kinetics. Such pore filling of the CO_2 capture process is a typical physical adsorption process by weak interactions of van der Waals forces and electrostatic interaction. Furthermore, surface O species can capture CO_2 molecules through hydrogen bonding or polarization, while surface N species enable us to bring some CO_2-philic sites to trap CO_2 by building acid−based interactions. As a result, these extra adsorption sites originating from surface heteroatoms greatly promote CO_2 capture efficiency, including CO_2 capture capacity and selectivity.

4. CONCLUSIONS

In summary, we report an innovative air-assisted pyrolysis strategy for designing N-rich ultramicroporous carbon spheres on a large scale using cross-linking urea-resorcinol-formaldehyde resins as precursors. We leverage porosity and the surface chemical environment by controlling the one-step pyrolysis process. The pore-forming mechanism of air-assisted pyrolysis method is unveiled in detail. The resultant materials exhibit uniform spherical morphology, well-interconnected hierarchical pore architecture, tailorable porosity, and adjustable surface heteroatom doping. Benefiting from the unique structure property, the obtained N-rich ultramicroporous carbon spheres present the outstanding CO_2 capture behaviors. The optimal material can achieve superior CO_2 uptakes of 3.79 and 5.42 mmol g^{-1} at 25 and 0 °C under 1.0 bar. Importantly, the ultrahigh CO_2/N_2 selectivity of 160 at 0.15 bar and 25 °C is obtained in the optimal NUCS-4−3 sample, and a satisfactory selectivity of 76 is still reached at 1.0 bar and 25 °C. Meanwhile, we ascertain the CO_2 adsorption mechanism of NUCS-*x*-*y* adsorbents, which is a pore-filling of monolayer physical adsorption process combining some extra relatively strong interactions from surface heteroatoms. The satisfactory CO_2 capture capacity, together with moderate Q_{st}, ultrahigh selectivity, and good regeneration, makes N-rich ultramicroporous carbon spheres a promising and adaptable porous adsorbent for postcombustion CO_2 capture and separation.

■ ASSOCIATED CONTENT

Supporting Information

The Supporting Information is available free of charge at https://pubs.acs.org/doi/10.1021/acsmaterialsau.4c00168.

SEM images of URF resins (Figure S1), the reaction process in pyrolysis (Figure S2), XRD pattern of URF resins (Figure S3), SEM images (Figure S4), DLS plots (Figure S5), FTIR spectra (Figure S6), XPS spectra (Figure S7), elemental contents of C, N, O (Figure S8), N species (Figure S9), ultramicropore size distribution (Figure S10), N_2 adsorption−desorption isotherms and pore size distribution (Figure S11), the correlations between CO_2 uptakes and porosity (Figure S12), the cumulative micropore volume of less than 1.0 nm (Figure S13), the correlations between CO_2 uptakes and surface heteroatoms (Figure S14), N_2 and CO_2 adsorption isotherms (Figure S15), IAST CO_2/N_2 selectivity at 0 °C (Figure S16), the comparison of selectivity (Figure S17), and Langmuir isotherm model fitting curves (Figure S18) (PDF)

■ AUTHOR INFORMATION

Corresponding Authors

Baocheng Yang − *Henan Provincial Key Laboratory of Nanocomposites and Applications, Institute of Nanostructured Functional Materials, Huanghe Science and Technology College, Zhengzhou, Henan 450006, China*; Email: baochengyang@infm.hhstu.edu.cn

Binbin Chang − *Henan Provincial Key Laboratory of Nanocomposites and Applications, Institute of Nanostructured Functional Materials, Huanghe Science and Technology College, Zhengzhou, Henan 450006, China*; orcid.org/0000-0001-6172-9952; Email: binbinchang@infm.hhstu.edu.cn

Authors

Man Liu − *Henan Provincial Key Laboratory of Nanocomposites and Applications, Institute of Nanostructured Functional Materials, Huanghe Science and Technology College, Zhengzhou, Henan 450006, China*

Weiwei Shi − *Henan Provincial Key Laboratory of Nanocomposites and Applications, Institute of Nanostructured Functional Materials, Huanghe Science and Technology College, Zhengzhou, Henan 450006, China*

Huili Liu − *Henan Provincial Key Laboratory of Nanocomposites and Applications, Institute of Nanostructured Functional Materials, Huanghe Science and Technology College, Zhengzhou, Henan 450006, China*

Yanzhen Guo − *Henan Provincial Key Laboratory of Nanocomposites and Applications, Institute of Nanostructured Functional Materials, Huanghe Science and Technology College, Zhengzhou, Henan 450006, China*

Complete contact information is available at:
https://pubs.acs.org/10.1021/acsmaterialsau.4c00168

Author Contributions

CRediT: **Man Liu** investigation, writing - original draft; **Weiwei Shi** investigation, resources; **Huili Liu** methodology; **Yanzhen Guo** investigation, methodology; **Baocheng Yang** supervision, writing - review & editing; **Binbin Chang** resources, supervision, writing - review & editing.

Notes

The authors declare no competing financial interest.

■ ACKNOWLEDGMENTS

This work was supported by the special fund project of Zhengzhou basic and applied basic research (ZZSZX202411), the Key Research Projects of Higher Education Institutions in Henan (25B430028), and Postgraduate Education Reform and Quality Improvement Project of Henan Province (YJS2022JD50).

■ REFERENCES

(1) Rohde, R. C.; Carsch, K. M.; Dods, M. N.; Jiang, H. Z. H.; McIsaac, A. R.; Klein, R. A.; et al. High-temperature carbon dioxide capture in a porous material with terminal zinc hydride sites. *Science* **2024**, *386*, 814−819.

(2) Wang, Y.; Qu, L.; Ding, H.; Webley, P.; Li, G. K. Distributed direct air capture of carbon dioxide by synergistic water harvesting. *Nat. Commun.* **2024**, *15*, 9745.

(3) Liu, G. Y.; Sun, S. Z.; Sun, H. M.; Zhang, Y.; Lv, J. B.; Wang, Y. H.; et al. Integrated CO_2 capture and utilization: A promising step contributing to carbon neutrality. *Carbon Capture Science & Technology* **2023**, *7*, No. 100116.

(4) Singh, G.; Lee, J.; Karakoti, A.; Bahadur, R.; Yi, J.; Zhao, D.; Albahily, K.; Vinu, A. Emerging trends in porous materials for CO_2 capture and conversion. *Chem. Soc. Rev.* **2020**, *49*, 4360−4404.

(5) Dunstan, M. T.; Donat, F.; Bork, A. H.; Grey, C. P.; Muller, C. R. CO_2 capture at medium to high temperature using solid oxide-based sorbents: fundamental aspects, mechanistic insights, and recent advances. *Chem. Rev.* **2021**, *121*, 12681−12745.

(6) Hu, X. Y.; Liu, L. B.; Luo, X.; Xiao, G. E.; Shiko, E.; Zhang, R.; Fan, X. F.; et al. A review of N-functionalized solid adsorbents for post-combustion CO_2 capture. *Applied Energy* **2020**, *260*, No. 114244.

(7) Khosrowshahi, M. S.; Mashhadimoslem, H.; Shayesteh, H.; Singh, G.; Khakpour, E.; Guan, X. W.; et al. Natural products derived porous carbons for CO_2 capture. *Adv. Sci.* **2023**, *10*, No. 2304289.

(8) Wang, L.; Ma, Y. K.; Liu, H. L.; Guo, Y. Z.; Yang, B. C.; Chang, B. B. Leveraging porosity and morphology in hierarchically porous carbon microtubes for CO_2 capture and separation from humid flue gases. *Sep. Purif. Technol.* **2025**, *354*, No. 128910.

(9) Siegelman, R. L.; Kim, E. J.; Long, J. R. Porous materials for carbon dioxide separations. *Nat. Mater.* **2021**, *20*, 1060−1072.

(10) Gao, X.; Yang, S.; Hu, L.; Cai, S.; Wu, L.; Kawi, S. Carbonaceous materials as adsorbents for CO_2 capture: synthesis and modification. *Carbon Capture Sci. Technol.* **2022**, 3, No. 100039.

(11) Edlabadkar, V. A.; Soni, R. U.; ud Doulah, A. B. M. S.; Owusu, S. Y.; Hackett, S.; Bartels, J. M.; Leventis, N.; Sotiriou-Leventis, C. CO_2 uptake by microporous carbon aerogels derived from polybenzoxazine and analogous all-nitrogen polybenzodiazine aerogels. *Chem. Mater.* **2024**, *36*, 1172−1187.

(12) Shi, W. W.; Yu, J.; Liu, H. L.; Gao, D. F.; Yuan, A. L.; Chang, B. B. Hierarchically nanoporous carbon for CO_2 capture and separation: roles of morphology, porosity, and surface chemistry. *ACS Appl. Nano Mater.* **2023**, *6*, 7887−7900.

(13) Tian, W.; Zhang, H.; Duan, X.; Sun, H.; Shao, G.; Wang, S. Porous carbons: structure-oriented design and versatile applications. *Adv. Funct. Mater.* **2020**, *30*, No. 1909265.

(14) Liu, R. S.; Shi, X. D.; Wang, C. T.; Gao, Y. Z.; Xu, S.; Hao, G. P.; Chen, S. Y.; Lu, A. H. Advances in post-combustion CO_2 capture by physical adsorption: from materials innovation to separation practice. *ChemSusChem* **2021**, *14*, 1428−1471.

(15) Singh, R.; Wang, L. Z.; Ostrikov, K.; Huang, J. Designing carbon-based porous materials for carbon dioxide capture. *Adv. Mater.* **2024**, *11*, No. 22022290.

(16) Wang, C. S.; Yan, B.; Zheng, J. J.; Feng, L.; Chen, Z. Z.; Zhang, Q.; Liao, T.; et al. Recent progress in template-assisted synthesis of porous carbons for supercapacitors. *Adv. Powder Mater.* **2022**, *1*, 100018.

(17) Yuan, X. Z.; Kumar, N. M.; Brigljevic, B.; Li, S. J.; Deng, S.; Byun, M.; Lee, B.; et al. Sustainability-inspired upcycling of waste polyethylene terephthalate plastic into porous carbon for CO_2 capture. *Green Chem.* **2022**, *24*, 1494−1504.

(18) Burrow, J. N.; Eichler, J. E.; Martinez, W. A.; Mullins, C. B. A data-driven approach to molten salt synthesis of N-rich carbon adsorbents for selective CO_2 capture. *Adv. Funct. Mater.* **2024**, *36*, No. 2306275.

(19) Kamran, U.; Park, S. J. Chemically modified carbonaceous adsorbents for enhanced CO_2 capture: A review. *J. Clean. Prod.* **2021**, *290*, No. 125776.

(20) Wang, X. L.; Alzayer, M.; Shih, A. J.; Bose, S.; Xie, H.; Vornholt, S. M.; et al. Tailoring hydrophobicity and pore environment in physisorbents for improved carbon dioxide capture under high humidity. *J. Am. Chem. Soc.* **2024**, *146*, 3943−3954.

(21) Li, Y. Q.; Yu, Y. F.; Liu, L.; Zhang, H. L.; Wang, G. X.; Chen, A. B. Synthesis of N-doped carbon spheres using extended stöber method for SO_2 adsorption. *Nano* **2017**, *12*, 1750004.

(22) Matsagar, B. M.; Yang, R. X.; Dutta, S.; OK, Y. S.; Wu, K. C. W. Recent progress in the development of biomass-derived nitrogen-doped porous carbon. *J. Mater. Chem. A* **2021**, *9*, 3703−3728.

(23) Wang, H. L.; Jin, Y. H.; Sun, N. N.; Zhang, W.; Jiang, J. Z. Post-synthetic modification of porous organic cages. *Chem. Soc. Rev.* **2021**, *50*, 8874−8886.

(24) Pagaduan, J. N.; Bhardwaj, A.; McCarty, T. Y.; Kraemer, S.; Kearney, C. J.; Watkins, J. J.; Emrick, T.; Katsumata, R. Fabrication of porous heteroatom-doped carbon networks via polymer-assisted rapid thermal annealing. *Adv. Funct. Mater.* **2024**, *34*, No. 2310296.

(25) Chang, B. B.; Shi, W. W.; Yin, H.; Zhang, S. R.; Yang, B. C. Poplar catkin-derived self-templated synthesis of N-doped hierarchical porous carbon microtubes for effective CO_2 capture. *Chem. Eng. J.* **2019**, *358*, 1507−1518.

(26) Chang, B. B.; Sun, L.; Shi, W. W.; Zhang, S. R.; Yang, B. C. Cost-efficient strategy for sustainable cross-linked microporous carbon bead with satisfactory CO_2 capture capacity. *ACS Omega* **2018**, *3*, 5563−5573.

(27) Wang, J. Y.; Li, X. T.; Tian, K.; Guo, W. C.; Zhang, B.; Zhang, J. M.; Li, M. R.; et al. Highly accessible 3D interconnected macro/microporous catechol-enriched carbon material to clarify its excellent pseudocapacitance. *ACS Materials Lett.* **2024**, *6*, 4571−4580.

(28) Pol, V. G.; Shrestha, L. K.; Ariga, K. Tunable, functional carbon spheres derived from rapid synthesis of resorcinol-formaldehyde resins. *ACS Appl. Mater. Interfaces* **2014**, *6*, 10649−10655.

(29) Wang, Y.; Fang, Y.; Wang, Y.; Wu, H.; Anpo, M.; Yu, J. C.; Wang, X. Plasma-enhanced chemical-vapor-deposition synthesis of photoredox-active nitrogen-doped carbon from NH_3 and CH_4 gases. *Angew. Chem., Int. Ed.* **2023**, *62*, No. e202307236.

(30) Zhang, J.; Xia, Z.; Dai, L. Carbon-based electrocatalysts for advanced energy conversion and storage. *Sci. Adv.* **2015**, *1*, No. e1500564.

(31) He, Z. S.; Zhao, A.; Liu, S. J.; Chen, Y. Q.; Liu, J.; Zhao, W. J.; et al. Preparation of nitrogen-containing chemicals from lignocellulosic biomass and nitrogen-rich organic solid waste by pyrolysis: Characteristics, reaction mechanisms, and feedstock interactions. *Chem. Eng. J.* **2024**, *496*, No. 153793.

(32) Xue, C. L.; Hao, W. M.; Cheng, W. P.; Ma, J. H.; Li, R. F. Effects of pore size distribution of activated carbon (AC) on CuCl dispersion and CO adsorption for CuCl/AC adsorbent. *Chem. Eng. J.* **2019**, *375*, No. 122049.

(33) Zhang, Y.; Shi, W.; Zhang, S.; Zhao, S.; Yang, B.; Chang, B. B. Rational design of *β*-cyclodextrins-derived hierarchically porous carbons for CO_2 capture: The roles of surface chemistry and porosity on CO_2 capture. *J. CO2 Utilization* **2022**, *66*, No. 102244.

(34) Tian, L.; Zhi, Y.; Yu, Q.; Xu, Q.; Demir, M.; Colak, S.; Farghaly, A. A.; Wang, L.; Hu, X. Enhanced CO_2 adsorption capacity in highly porous carbon materials derived from melamine-formaldehyde resin. *Energy Fuels* **2024**, *38*, 13186−13195.

(35) Tang, Z.; Gao, J.; Zhang, Y.; Du, Q.; Feng, D.; Dong, H.; Peng, Y.; Zhang, T.; Xie, M. Ultra-microporous biochar-based carbon adsorbents by a facile chemical activation strategy for high-performance CO_2 adsorption. *Fuel Process. Technol.* **2023**, *241*, No. 107613.

(36) He, S.; Chen, G.; Xiao, H.; Shi, G.; Ruan, C.; Ma, Y.; Dai, H.; Yuan, B.; Chen, X.; Yang, X. Facile preparation of N-doped activated carbon produced from rice husk for CO_2 capture. *J. Colloid Interface Sci.* **2021**, *582*, 90−101.

(37) Wang, H.; Wang, H.; Liu, G.; Yan, Q. In-situ pyrolysis of Taihu blue algae biomass as appealing porous carbon adsorbent for CO_2 capture: Role of the intrinsic N. *Sci. Total Environ.* **2021**, *771*, No. 145424.

(38) Karve, V. V.; Espín, J.; Asgari, M.; Van Gele, S.; Oveisi, E.; Queen, W. L. N-containing carbons derived from microporous coordination polymers for use in post-combustion flue gas capture. *Adv. Funct. Mater.* **2023**, *33*, No. 2212283.

(39) Yu, J.; Xiao, J. F.; Wang, Y.; Zhang, T. C.; Li, J.; He, G.; Yuan, S. N, P co-doped cellulose-based carbon aerogel: A dual-functional porous material for CO_2 capture and supercapacitor. *Sep. Purif. Technol.* **2025**, *359*, No. 130569.

(40) Liu, D.; Shao, L.; Zhan, P.; Zhang, L.; Wu, Z.; Wang, J.; Ma, X.; Huang, J. Insights into mechanochemical assisted preparation of lignin-based N-doped porous carbon with tunable porosity and ultrahigh surface oxygen content for efficient CO_2 capture. *Sep. Purif. Technol.* **2024**, *347*, No. 127657.

(41) Liu, C.; Wang, J.; Zhang, S.; Wei, C.; Cao, L.; Zhou, Y.; Zhang, J.; Zhang, S. Ultramicropore-rich N-doped porous biochar from discarded cigarette butts for efficient CO_2 capture with ultra-high adsorption capacity and selectivity. *Sep. Purif. Technol.* **2025**, *358*, No. 130205.

(42) Li, H.; Niu, J. B.; Tay, K. J.; Tan, M. C.; Low, H. Y. Sustainable dual-template fabrication of hierarchical pore structure for enhanced and stable CO_2 capture. *ACS Sustainable Chem. Eng.* **2024**, *12*, 2911−2920.

(43) Albeladi, N.; Mokaya, R. Modulating the porosity of N-doped carbon materials for enhanced CO_2 capture and methane uptake. *J. Mater. Chem. A* **2024**, *12*, 21025−21040.

(44) Zhang, Z.; Zhou, J.; Xing, W.; Xue, Q.; Yan, Z.; Zhuo, S.; Qiao, S. Z. Critical role of small micropores in high CO_2 uptake. *Phys. Chem. Chem. Phys.* **2013**, *15*, 2523−2529.

(45) Modak, A.; Jana, S. Advancement in porous adsorbents for post-combustion CO_2 capture. *Microporous Mesoporous Mater.* **2019**, *276*, 107−132.

(46) Saha, D.; Kienbaum, M. J. Role of oxygen, nitrogen and sulfur functionalities on the surface of nanoporous carbons in CO_2 adsorption: A critical review. *Microporous Mesoporous Mater.* **2019**, *287*, 29−55.

(47) Singh, G.; Kim, I. Y.; Lakhi, K. S.; Joseph, S.; Srivastava, P.; Naidu, R.; Vinu, A. Heteroatom functionalized activated porous biocarbons and their excellent performance for CO_2 capture at high pressure. *J. Mater. Chem. A* **2017**, *5*, 21196−21204.

(48) Farmahini, A. H.; Krishnamurthy, S.; Friedrich, D.; Brandani, S.; Sarkisov, L. Performance-based screening of porous materials for carbon capture. *Chem. Rev.* **2021**, *121*, 10666−10741.

(49) Madani, S. H.; Hu, C.; Silvestre-Albero, A.; Biggs, M. J.; Rodriguez-Reinoso, F.; Pendleton, P. Pore size distributions derived from adsorption isotherms, immersion calorimetry, and isosteric heats: a comparative study. *Carbon* **2016**, *96*, 1106−1113.